Article

Temperature Estimation in Lithium-Ion Cells Assembled in Series-Parallel Circuits Using an Artificial Neural Network Based on Impedance Data

Marco Ströbel * , **Vikneshwara Kumar and Kai Peter Birke**

Electrical Energy Storage Systems, Institute for Photovoltaics, University of Stuttgart, Pfaffenwaldring 47, 70569 Stuttgart, Germany; st176769@stud.uni-stuttgart.de (V.K.); peter.birke@ipv.uni-stuttgart.de (K.P.B.)
* Correspondence: marco.stroebel@ipv.uni-stuttgart.de

Abstract: Lithium-ion cells are widely used in various applications. For optimal performance and safety, it is crucial to have accurate knowledge of the temperature of each cell. However, determining the temperature for individual cells is challenging as the core temperature may significantly differ from the surface temperature, leading to the need for further research in this field. This study presents the first sensorless temperature estimation method for determining the core temperature of each cell within a battery module. The accuracy of temperature estimation is in the range of $\Delta T \approx 1$ K. The cell temperature is determined using an artificial neural network (ANN) based on electrochemical impedance spectroscopy (EIS) data. Additionally, by optimizing the frequency range, the number of measurement points, input neurons, measurement time, and computational effort are significantly reduced, while maintaining or even improving the accuracy of temperature estimation. The required time for the EIS measurement can be reduced to 0.5 s, and the temperature calculation takes place within a few milliseconds. The setup consists of cylindrical 18,650 lithium-ion cells assembled into modules with a 3s2p configuration. The core temperature of the cells was measured using sensors placed inside each cell. For the EIS measurement, alternating current excitation was applied across the entire module, and voltage was measured individually for each cell. Various State of Charge (SoC), ambient temperatures, and DC loads were investigated. Compared to other methods for temperature determination, the advantages of the presented study lie in the simplicity of the approach. Only one impedance chip per module is required as additional hardware to apply the AC current. The ANN consists of a simple feedforward network with only one layer in the hidden layer, resulting in minimal computational effort, making this approach attractive for real-world applications.

Keywords: lithium-ion batteries; temperature estimation; sensorless temperature measurement; artificial intelligence; artificial neural network

1. Introduction

The market for electric vehicles containing lithium-ion batteries (LIBs) is growing steadily. The forecasts for the next few years predict further significant growth [1]. Nonetheless, a significant demand remains for further research and development within the realm of LIBs, aiming to enhance both performance and safety. Precise knowledge of the cell temperature is crucial to operate them within the optimal range, as operation outside the specified temperatures causes accelerated cell aging. Lithium plating can occur at low temperatures due to reduced reaction kinetics, resulting in damage to the solid electrolyte interface (SEI) and loss of electrolyte and lithium when the SEI is repaired. At excessively high temperatures, decomposition of cell components and accelerated side reactions may occur [2]. Hence, ensuring thermal safety is vital during the progression of lithium-ion battery pack technology. In the most severe scenario, a cell malfunction can trigger a thermal runaway event. The thermal runaway of one cell can spread to surrounding cells and cause propagation throughout the battery pack [3,4]. The Chinese authorities have

required that the driver of the vehicle receive a warning in the event of a thermal runaway. In this case, the driver must receive the notification 5 min before the first effects of smoke or heat inside the vehicle [5].

The United Nations Global Technical Regulation on Electric Vehicle Safety (GTR EVS), specifically Sections I. E. 7 c 112, II. 5.3.3, and II. 7.2.3, outlines the need for a functional safety mechanism. This mechanism is expected to effectively detect the occurrence of a thermal runaway in a single cell of the traction battery, immediately notify the problem to the driver, and give all passengers a few minutes to safely exit the vehicle before a potentially dangerous situation arises [6,7].

For this reason, it is essential to detect the current cell temperature as accurately as possible in order to monitor the cells and switch them off in the event of a fault. It would be optimal if the temperature of each individual cell within a module or a battery pack could be determined.

There are various methods used to determine the cell temperature [8–12]. A comprehensive overview is presented by Raijmakers et al. [13]. The most accurate method would be to place temperature sensors inside each cell. However, this approach is not feasible from an economic and technical standpoint [2,14]. A technically simpler solution is to attach sensors to the surface of the cells. However, since the temperature inside the cell can be significantly higher under load than on the surface, the actual cell temperature is only captured with a delay or complex thermal models are required [12,15–17]. Furthermore, the accuracy of temperature measurement is influenced by the thermal contact and positioning of the temperature sensors. It is important to note that not all cells are outfitted with sensors. As a result, the design of the pack must consider this factor to effectively detect potential hotspots [18]. As the temperature determination using internal temperature sensors is too complex and external temperature sensors are not accurate due to time delays, there are various approaches to estimate the temperature based on the electrical parameters of the cell. Thermal models attempt to determine heat generation using current, voltage, and ambient data. These models are capable of predicting cell temperature with sufficient accuracy [19–21]. However, these methods also come with several challenges. Since the calculations often rely on the assumption that heat generation is formed by the product of current squared and internal resistance, the resistance must be accurately known. However, it is dependent on cell temperature, aging condition, and state of charge. Furthermore, the measurement data must be continuously recorded and fed to the model to make reliable predictions. This results in high data traffic and computational effort.

Impedance-based methods overcome many of these challenges. The impedance spectrum represents a characteristic pattern that can be associated with a particular condition. The pioneering work of Srinivasan et al. recognized a relationship between impedance at frequencies ranging from 40 to 100 Hz and temperature. It is noteworthy that other parameters such as SoC and state of health (SoH) have little influence on impedance within the temperature range of −20 °C to 66 °C [22]. Schmidt et al. show that using the real part of the impedance measurement at elevated frequencies allows accurate precise sensorless determination of the average internal temperature within a prismatic cell. This is particularly advantageous as the time constant exhibits a notably diminished correlation with the SoC, allowing improved temperature estimation even in cases where the SoC is unknown [23]. Richardson et al. investigated the impact of internal thermal gradients on impedance. By combining impedance measurements with the Kalman filter (KF), it is possible to estimate the core temperature of LIBs. This integrated approach not only enables the detection of internal hotspots without any time delays but also provides an estimation of the volume-average temperature [14]. The pronounced correlation between impedance and temperature is illustrated in Figure 1. A noticeable decrease in impedance response is evident with rising temperatures, as observed in the measurements carried out by the researchers. The EIS measurements were executed on LG INR18650MH1 cells across various temperature levels. Further information regarding the experimental procedure can be found in the specified Section 2.2.
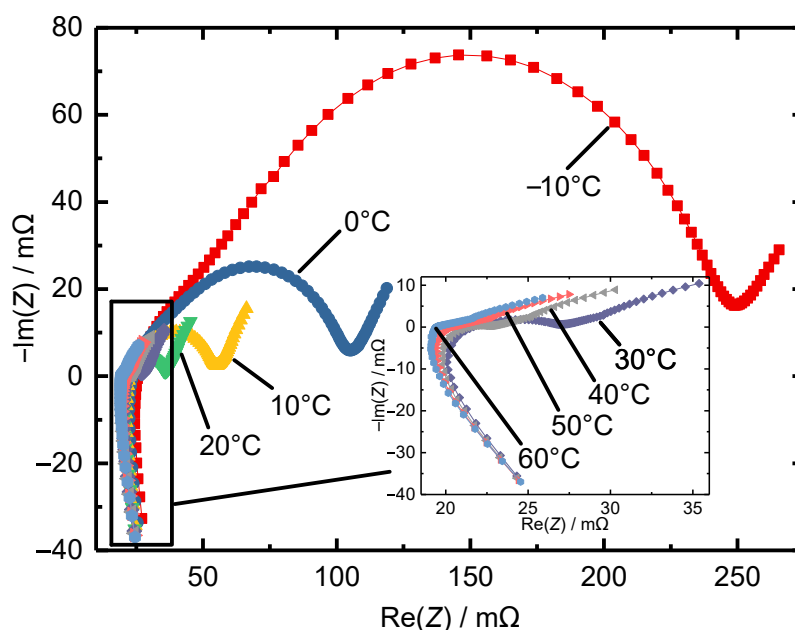
Figure 1. Nyquist plot of an LG INR18650MH1 cell at different temperatures from −10 °C to 60 °C. The impedance spectrum exhibits a strong dependence on the cell temperature.

As a result, the impedance-based method enables the determination of the average cell temperature without the need for temperature sensors [24]. In their study, Li et al. offer a comprehensive overview of different impedance-based methods used to indicate temperatures in LIBs [11].

Almost all publications found in the literature either show a correlation between a measured quantity and the desired state of a single cell or focus on temperature determination in individual cells. However, there are very few publications that deal with temperature determination using impedance spectroscopy of individual cells that have been connected in series or parallel to modules or battery packs. One of the reasons for this is the so-called cross-talk interference. The common approach is often to perform separate EIS measurements with an impedance chip on each cell in a connection. This leads to errors in the measurement due to the influence of neighboring cells [25]. Another challenge lies in the selection of parameters used for temperature determination and the data processing approach. The impedance spectrum of a cell depends on numerous factors. Besides the strong correlation between temperature and impedance, the state of charge and aging condition also influence the impedance spectrum. Beelen et al. compared several approaches for temperature determination and demonstrated in their study the significance of choosing the optimal parameters [26].

The presented study utilizes ANNs as they are capable of independently learning and representing multidimensional systems. A significant advantage of this methodology is its automatability and applicability to different cell chemistries. In the literature, there are only a few available studies that address temperature estimation using ANNs. Some of these studies combine physical models with ANNs to improve temperature estimation [27], while others are based on a nonlinear autoregressive exogenous ANN and time series data, such as current and ambient temperature [28]. Additionally, some studies employ ANN-based methods for SoC or SoH estimation [29–32].

Combining impedance data with ANNs has been the focus of only a few studies. Messing et al. included impedance data for both the parameterization of the equivalent circuit and as input for the ANN [33]. However, the majority of approaches still rely on methods that require significant computational effort, such as solving partial differential equations, fitting physical models, or analyzing time series data.

The combination of impedance data with simple ANNs, requiring low computational effort, for temperature estimation in individual cells was previously presented by the

authors in an earlier publication [34]. It was shown that temperature determination on a single cell using ANN based on impedance data can be performed with high accuracy. The next step, which is worked out in this publication, is the determination of the temperature of each individual cell within a series-parallel circuit. To overcome the challenge of cross-talk interference, a galvanostatic AC excitation is applied across the entire module, and the voltage at each cell is measured. This approach offers the significant advantage of requiring only a few additional hardware components. As it is necessary for safety reasons to measure the voltage of each individual cell in a module in order to comply with the permissible voltage limits, no further voltage sensors are required. For AC excitation, only one additional impedance chip per module is required.

The aim of this publication is to determine the temperature of each individual cell within a circuit consisting of lithium ion cells connected in series and parallel. From the directly measurable quantities of the EIS measurements (voltage, current, time), the real and imaginary parts of the impedance are calculated. Data processing is performed using ANNs, where the real and imaginary parts of the impedance at different frequencies serve as input data for the ANN to estimate the temperature.

According to the authors' knowledge, this is the first publication presenting temperature estimation in individual cells for a connection of multiple cells without temperature sensors. In Section 2, the authors describe cell preparation, data acquisition, and the architecture of the ANN. Section 3 subsequently showcases the outcomes of the temperature estimation.

2. Materials and Methods

Temperature sensors were inserted into the center of cylindrical lithium-ion cells to measure the core temperature. The prepared cells were then connected in a 3s2p configuration. Impedance measurements were conducted within a temperature chamber at different temperatures and state of charge conditions, using different superimposed DC currents, while measuring the core temperature. To simulate real-world applications, electrochemical impedance spectroscopy measurements were performed immediately after reaching the SoC without relaxing the cells. During the EIS measurement, the cell was continuously charged/discharged. The recorded EIS measurements, along with their corresponding core temperatures, were divided into two datasets: a training dataset and a test dataset. The training dataset is used to train the ANN, then validated using the test dataset to ensure its accuracy in estimating temperatures from impedance measurements.

2.1. Cell Preparation

For the experiments, LG INR18650MH1 lithium-ion cylindrical cells were used, with a nominal voltage of $U_N = 3.6$ V and a capacity of $Q = 3200$ mAh. Since the cells were new, initially, 20 full cycles were performed as we observed slight changes in the impedance spectrum during the first cycles. Subsequently, the cells were discharged to $U_{min} = 2.5$ V using a CC/CV (constant current/constant voltage) method. The preparation with temperature sensors was carried out in an MBraun LabStar glovebox (Germany) under an argon atmosphere. The water and oxygen content in the glovebox was less than 0.5 ppm. As shown in Figure 2, the core of the cell is hollow. Since the negative pole consists only of the bottom of the cell cup and the current collector, it was suitable for the preparation with the temperature sensor. The cells were opened in the middle of the negative pole using a drill (diameter $d = 1.3$ mm). Subsequently, two negative temperature coefficient (NTC) sensors (NTC Thermistor 10k Perle SC30F103V by Amphenol Thermometrics, United Kingdom) were inserted into each cell.

The temperature sensors used in the experiment have a diameter of $d_{sens} = 0.81$ mm and are coated with a polyimide that can withstand the electrolyte for a sufficient period of time. After inserting the sensors, the opening was sealed (the first setups used the two-component adhesive UHU PLUS ENDFEST by UHU from Germany, and later the UV-light sensitive adhesive Polytec UV 2133 from Polytec PT GmbH Germany). The adhesive from

UHU was left to dry for 24 h under an argon atmosphere. Polytec's adhesive is solid after only a few seconds when irradiated with UV light (wavelength approximately 400 nm). After the cell preparation, electrochemical impedance spectroscopy measurements were conducted before and after cell preparation to ensure that the cells were not damaged during the preparation process.

The prepared cells were connected in a 3s2p configuration using soldering. A schematic representation of the setup is shown in Figure 3.
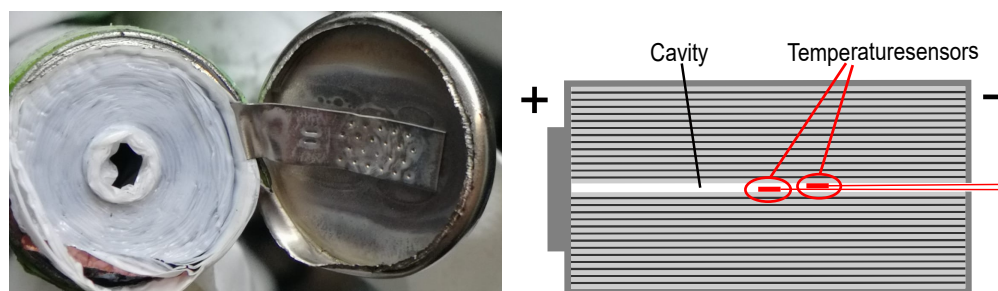
Figure 2. Left: An opened 18,650 cylindrical cell. In the center of the winding, there is a cavity, and the negative pole consists only of a metal bottom and the current collector. **Right**: Schematic representation of cell preparation with temperature sensors.
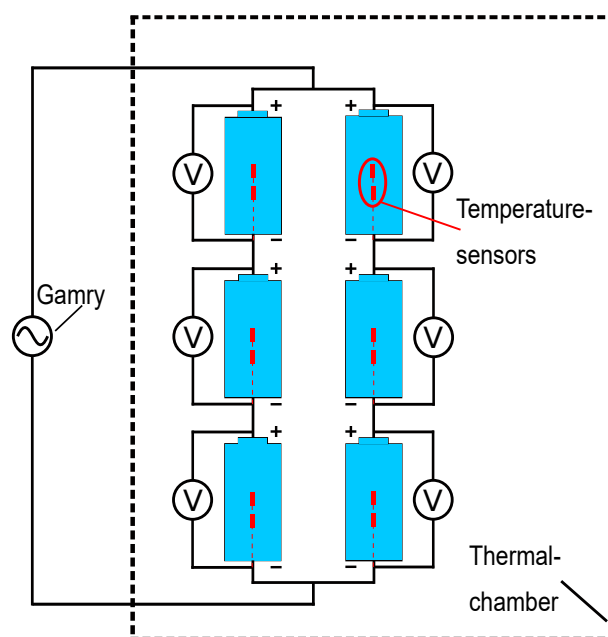
Figure 3. Schematic representation of the 3s2p experimental setup.

The setup consists of two series connections, each with three cells, that are connected in parallel. The voltage is directly measured from each individual cell. Each cell is equipped with two temperature sensors, which are calibrated after the preparation in a temperature chamber of type ICP 110 (temperature accuracy: $\Delta T = \pm 0.1$ K) manufactured by Memmert (Germany). For calibration, the entire setup is adjusted to different temperatures between $10\,°C < T < 50\,°C$ inside the temperature chamber. After a relaxation time of 2 h, the sensor measurement value is determined for calibration. A separate measuring system was developed to read and analyze the sensor values. The resistance of the sensor was measured using a voltage divider setup with an SL1TTE1002F resistor from KOA Speer Electronics Inc. The analog data were converted into a digital format using an ADS1115 module by Adafruit. An Arduino Mega 2560 was used to process the data and store it on a Micro-SD card. The measuring system has a logging capability of approximately 4.5 data points per second. Following the recording process, the digitized data was transformed into

temperature values using the sensor's manual as reference. A more detailed description of the system is described in Ref. [35]. All further measurements are also conducted within the temperature chamber. The AC is applied to the entire circuit using the Potentiostat reference 3000 AE by Gamry (Pennsylvania, USA). The voltage measurement from the individual cells is also performed using the Potentiostat by Gamry.

2.2. Electrochemical Impedance Spectroscopy

EIS allows for gathering extensive information about an electrochemical system without causing any damage to it. The impedance is composed, according to Equation (1), of the complex current, complex voltage, and phase shift. Subsequently, the real R and imaginary jX components of the impedance can be calculated.

$$\underline{Z} = \frac{\underline{u}}{\underline{i}} = R + jX \tag{1}$$

The system is subjected to a sinusoidal excitation, and the phase-shifted response is measured. By introducing AC currents at various frequencies (typically ranging from 10 kHz to 10 mHz), an electrochemical impedance spectrum is generated. The outcomes of an EIS measurement are graphed on a Nyquist plot. As previously described, the cells were additionally charged/discharged during the EIS measurements to simulate realistic scenarios. This led to the selection of the galvanostatic mode for EIS measurements, ensuring the conservation of charge carriers. The frequency range of operation was configured spanning from $f = 10$ kHz down to $f = 1$ Hz, encompassing 15 frequencies within each decade for a cumulative count of 61 frequencies. Furthermore, this frequency band was delimited to encompass the variations in charge that might arise from the application of potentially superimposed current. To strike a balance, an alternating current with a C-rate of 1/20 C was employed for all measurements. In this context, capacity denotes the circuit's overall capacity. This choice guarantees linearity and a favorable signal-to-noise ratio. The SoC was set using a CC/CV charge/discharge (current limit C/100) for each measurement. The target voltage for SoC setting corresponds to the open circuit potential.

Various measurement series were conducted. In the first series, called "Setup 1", a 3s2p configuration was examined at a constant SoC of 70% without overlaid DC current. For the training data, EIS measurements were performed between $T_1 = 10\,°\text{C}$ and $T_2 = 50\,°\text{C}$ in steps of $\Delta_T = 2.5\,°\text{C}$ at a constant ambient temperature. For the test data, the temperature chamber was initially set to 50 °C and then cooled down to 10 °C. EIS measurements were conducted on the cells during the cooling process, generating a temperature gradient of up to $\Delta_T = 5\,°\text{C}$ between the cell surface and the cell core. This was intended to simulate the temperature gradient within cells under high currents.

For the second series, called "Setup 2", measurements were conducted on two 3s2p configurations to verify the reproducibility. The temperature chamber was set to different constant temperatures for these measurements. EIS measurements were performed for different SoC values between 10% and 90% in steps of 20%. During the EIS measurements, various DC currents up to C-rate $= C/2$ were applied in charging and discharging directions to simulate a realistic operation. During these investigations, a relaxation period of 2 h was observed only after changing the temperature of the temperature chamber. The cells were not relaxed during the remaining measurements.

2.3. Artificial Neural Network Architecture

In this study, the ANN employed is based on the MATLAB Neural Network Toolbox. The structure is characterized by a feed-forward architecture, featuring a sole output contingent upon the relevant state (temperature), and is illustrated in Figure 4.

The ANN can be divided into three parts. The input layer neurons receive the input data. In this study, the input data consists of the real and imaginary parts of the impedance spectrum at various frequencies, and optionally information about the SoC and the applied DC current. During training, the output layer neuron is given the target value (tempera-

ture) that the cell had during the impedance measurement. After the training phase, the test phase follows, during which the network's output neuron represents the calculated temperature. To validate the methodology, the calculated temperature is compared with the actually measured temperature. The hidden layer is the core of the network where the "magic" happens. During the training process, the network adjusts the weights of the neurons iteratively until it can accurately represent the investigated system. For the purpose of identifying the most suitable number of neurons, a grid search method is utilized. This involves gradually augmenting the count of neurons within the hidden layer, until the enhancement in prediction accuracy plateaus, while ensuring the preservation of generalization capability. The number of neurons in the hidden layer will be reported separately for each investigated case in the discussion. To perform computations in the hidden layers, a hyperbolic tangent sigmoid transfer function (tansig) is used. This transfer function allows for non-linear transformations, which is essential for the network to learn complex relationships in the data and make accurate predictions, defined as:

$$tansig(n) = \frac{2}{(1 + exp(-2n)) - 1}$$

For the exploration of the optimal parameters of the ANN, the Bayesian regularization-backpropagation algorithm is employed in all tests. The evaluation of prediction accuracy involves the utilization of root mean square error and the coefficient of determination. The code for this assessment was created using the ANN toolbox. The number of hidden layers is limited to 1, as it has already yielded very good results. A low number of hidden layers also has the advantage of requiring less computational power. The number of neurons in the hidden layer is varied between 3 and 10 neurons for each experimental setup. For each neuron configuration, 3 training runs are conducted. The training data is not divided into smaller batches but is presented as a whole to the network. The maximum number of training iterations is limited to 10,000. Training is terminated if there is no improvement in 100 consecutive iterations.
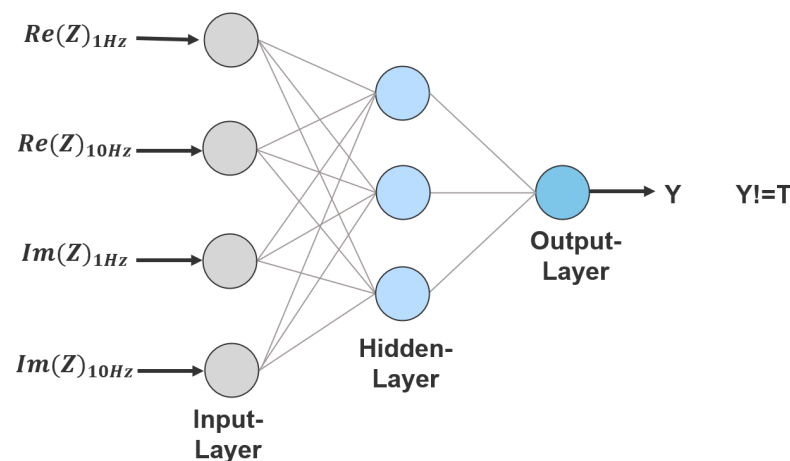
Figure 4. Diagram illustrating the employed ANN, where inputs consist of the real and/or imaginary components of impedance measurements.

3. Results

In this section, we first discuss the preceding characterization and analysis of the impedance data, which serves for selecting the optimal parameters. Subsequently, the results of Setup 1 are presented, where various temperatures were investigated at a constant SoC. This is followed by the presentation of Setup 2, which demonstrates temperature determination with varying SoCs and overlaid DC currents during the EIS measurements.

3.1. Preliminary Characterization

Figure 5 exemplifies the results of the EIS measurements before and after the sensor preparation. In all cells, the ohmic resistance is approximately 1 mΩ higher after the preparation compared to before. This increase was observed in all cells. This rise in resistance is likely due to the drilling of the negative pole, which also punctures the current collector tab of the electrode, leading to a reduction in the current-conducting area. The increase in the ohmic resistance of the cells due to the preparation by 1 mΩ corresponds to an increase of approximately 2.5%. Considering that the end of life criterion of a cell is only reached with a resistance increase of 200%, a 2.5% increase is negligible. Additionally, as shown in Figure 1, it becomes evident that the charge transfer resistance is temperature-dependent, particularly affected by temperature fluctuations. However, this is not compromised during the preparation involving the sensors.
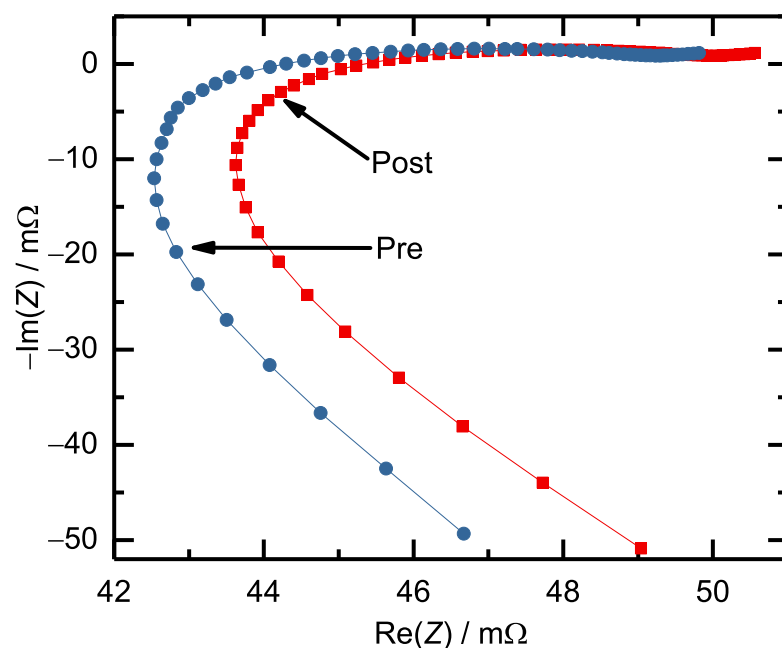
Figure 5. Nyquist plots of a cell before and after the preparation with a temperature sensor.

Furthermore, the impedance spectra recorded at the beginning and the end of the data collection were compared. However, no changes were observed, so they are not presented here. Since there were no changes, it is assumed that the cells remained sealed after closure, and no significant further aging occurred.

Figure 6 depicts the Bode plot of a cell at a constant temperature of $T = 25\,°C$ for different SoC levels.

In the Bode plot, the real part (top) and the imaginary part (bottom) of the impedance are plotted against frequency. In both representations, it is evident that the SoC has only a minimal influence on the impedance at frequencies above approximately 50 Hz. However, at lower frequencies, there is a more pronounced correlation between impedance and SoC. In Figure 7, the Bode plot for different overlaid DC currents during the EIS measurement is presented. In this case, the cell was charged or discharged with the specified C-rate while simultaneously conducting an EIS measurement. The ambient temperature was kept constant at 25 °C, and the SoC was set to 50% for each measurement. The results demonstrate that overlaid DC currents have only a minor influence on the impedance spectrum of a cell.
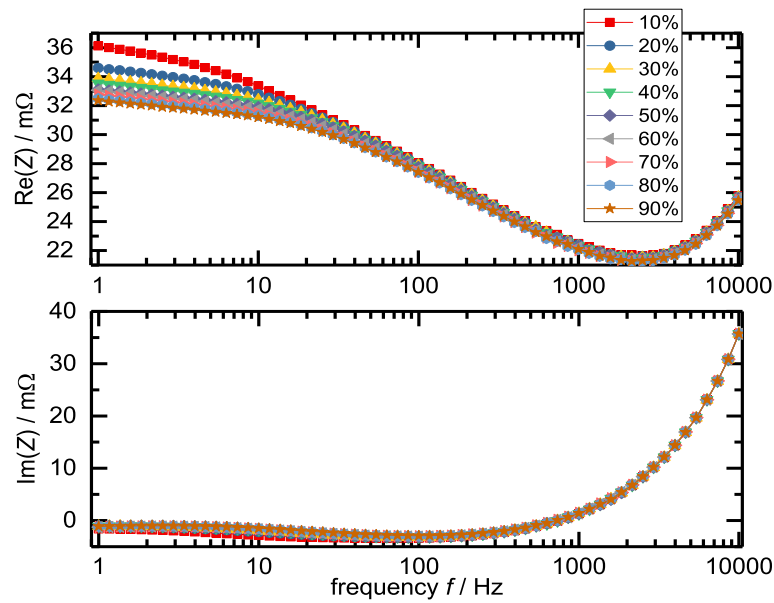
Figure 6. Bode plot at 25 °C with different SoC between 10% and 90%.
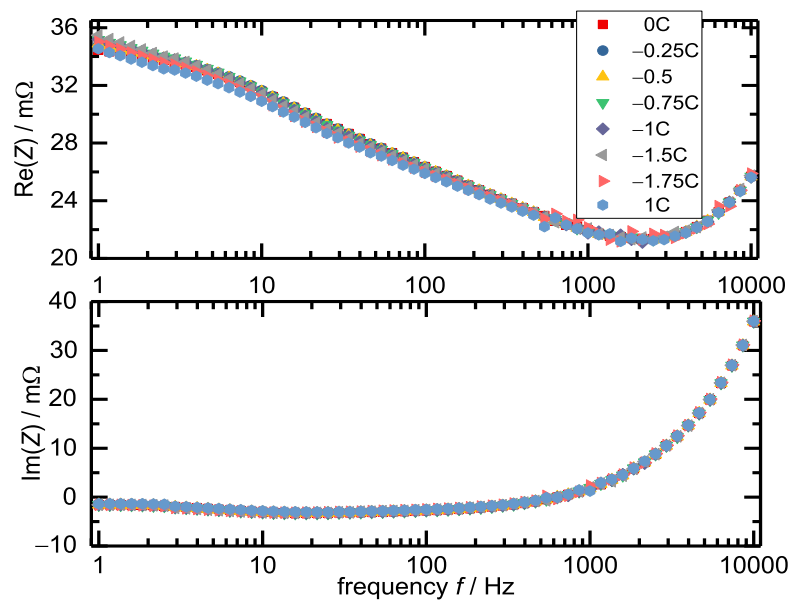
Figure 7. Bode plot at 25 °C and 50% SoC with different DC currents during the EIS measurement at C-rates between 1 C and −1.75 C.

The Bode plot for different temperatures at 70% SoC and without DC currents is shown in Figure 8. As known from the literature, there is a strong correlation between temperature and cell-impedance. At frequencies above 1 kHz, the influence of temperature on the impedance becomes minimal. The real part of the impedance exhibits strong temperature dependence at lower frequencies, which decreases significantly with increasing frequency.

The imaginary part shows particularly strong temperature dependence in the range between 800 Hz and approximately 1 Hz. By examining the frequency analysis, the range of frequencies used can be significantly narrowed down. The temperature analysis shows that the impedance is only slightly dependent on temperature for frequencies above 1 kHz, providing almost no information for the ANN. The frequency analyses for the SoC and DC current dependence of the impedance indicate an influence for frequencies below approximately 30–50 Hz.

The influences of temperature and SoC on the impedance of a lithium-ion cell, described so far, become even more evident in Figure 9. Here, impedance data for SoCs of 10%, 50%, and 90% are presented at ambient temperatures of 20 °C and 50 °C.
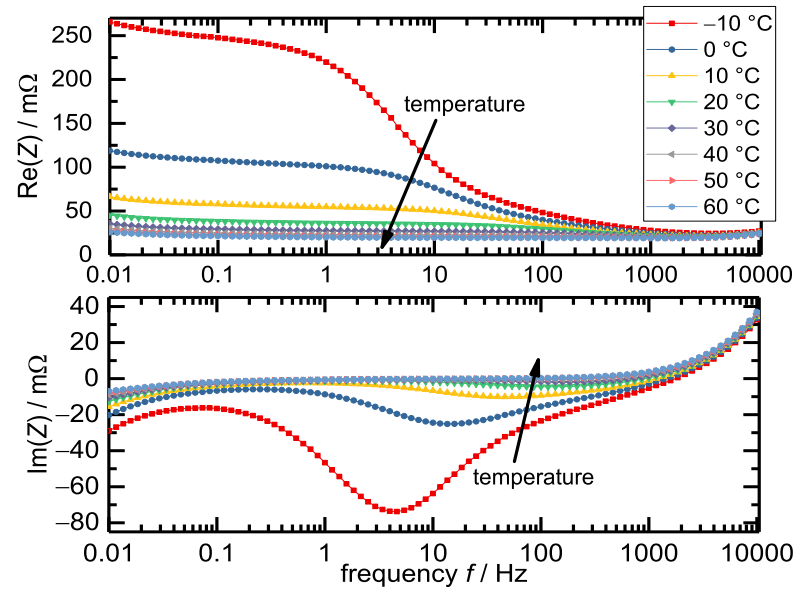
Figure 8. Bode plot at 70% SoC with different temperature between −10 °C and 60 °C.
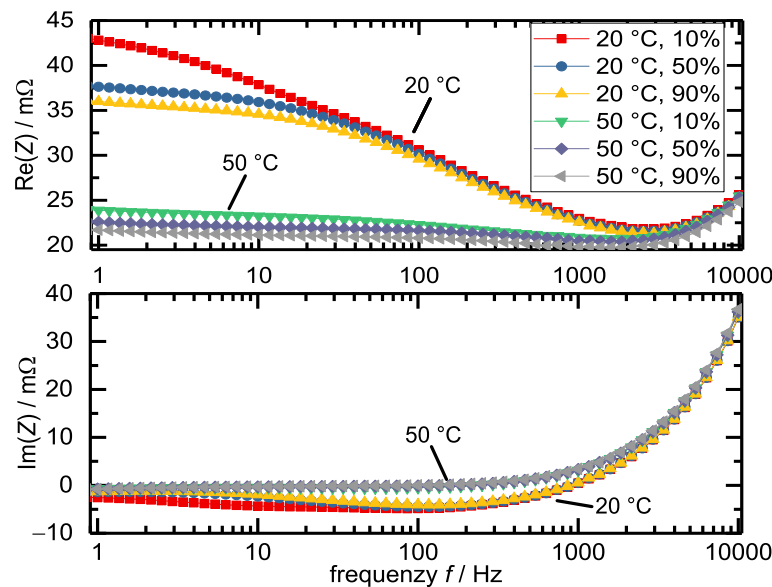
Figure 9. Bode plot for SoCs of 10%, 50%, and 90% at ambient temperatures of 20 °C and 50 °C.

It is clearly evident that the influence of temperature on impedance is significantly stronger than the influence of SoC. To verify these findings, the ANNs will be initially provided with information for all frequencies between 10 kHz and 1 Hz, and then for frequencies between 800 Hz and 30 Hz.

3.2. Temperature Estimation: Setup 1

Setup 1 consists of a 3s2p configuration. The training data was generated at constant temperatures, while for the test data, the temperature chamber was cooled down to create a temperature gradient between the cell core and surface. The gradient reached up to $\Delta_T = 5$ °C. The results of the temperature estimation are shown in Figure 10. The ANN was provided with the real and imaginary parts of the impedance for all measured frequencies

between 10 kHz and 1 Hz. The SoC was kept constant at 70%, and no DC current was applied. The collective root mean square error (RMSE) is below 1 K. The highest RMSE observed for an individual temperature estimation is approximately 1.4 K.
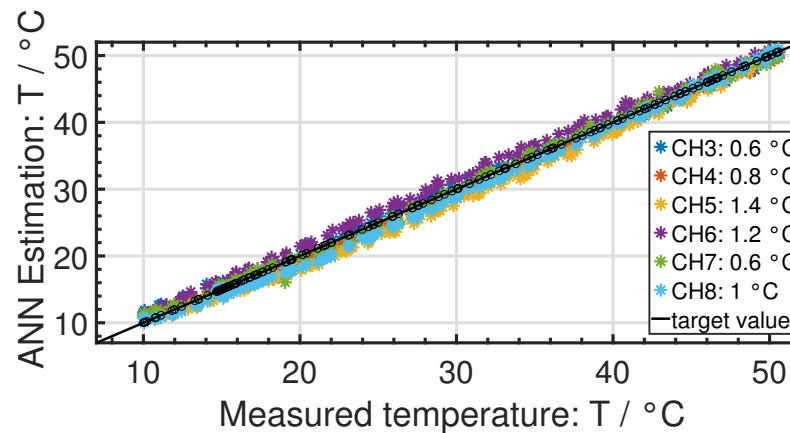
Figure 10. The plot depicts the estimated temperature against the measured temperature, with a black line serving as a guide for the target value. For temperature estimation, both the real and imaginary parts of all 61 frequencies were used. The frequency range spans from 10 kHz to 1 Hz. The overall RMSE is less than 1 K. The legend indicates the RMSE for each individual cell. The cells are connected in a 3s2p configuration.

On the y-axis, the temperature estimated by the ANN is shown, while the values on the x-axis represent the actually measured temperatures. The black line is a guide for the eye. Ideally, all estimated values would lie on the black line. The results indicate that, in general, the ANN is capable of estimating the temperature from a corresponding EIS spectrum for a multi-cell system. Figure 11 depicts the training progression of the ANN. The training process is halted when the Mean Squared Error (MSE) does not continue to decrease over 100 consecutive iterations. The minimum was reached after 464 iterations, and the training was stopped after 564 iterations. The MSE trajectory was employed to determine an optimal ANN setup. The showcased outcomes are derived from a Bayesian regularization-backpropagation neural network, featuring a solitary hidden layer housing 7 neurons. Introducing more than 7 neurons to the hidden layer often results in overfitting.
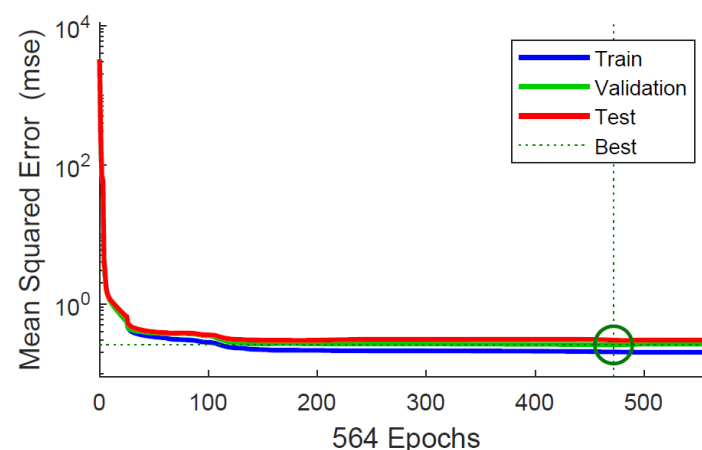
Figure 11. The plot showcases the evolution of MSE throughout the training epochs for temperature estimation of the 3s2p arrangement. A minimum MSE was reached after 464 epochs, and after an additional 100 epochs without a further reduction in MSE, the training was concluded.

In the previous subsection, a frequency analysis was conducted for the different influencing factors (temperature, SoC, DC current). For temperature estimation, the frequency range between 800 Hz and 30 Hz was identified as particularly suitable. From

the impedance data generated for setup 1, the real and imaginary parts for the mentioned frequency range were extracted and provided to the ANN. The results are depicted in Figure 12.
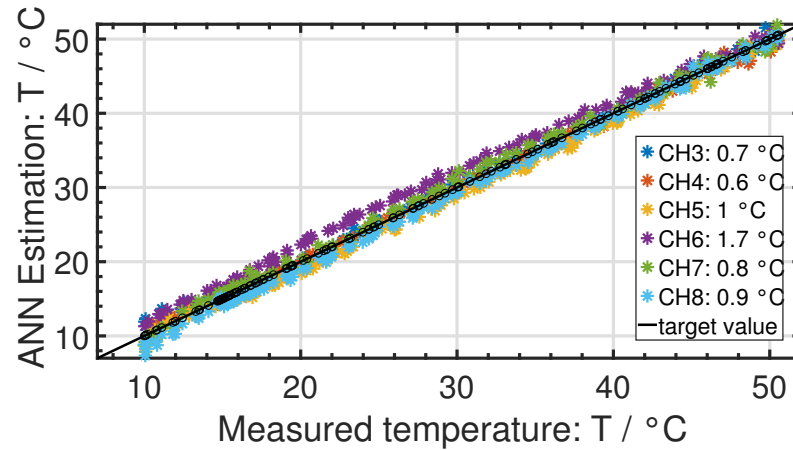
Figure 12. The plot displays the estimated temperature against the measured temperature, with a black line as a guide representing the target value. For training and testing the ANN, the frequency range was restricted to 800 Hz to 30 Hz, resulting in a reduction of the number of examined frequencies from 61 to 21. The overall RMSE for is less than 1 K. The legend indicates the RMSE for each individual cell.

The global RMSE remains below 1 K. The highest RMSE observed for an individual temperature estimation is approximately 1.7 K. The number of neurons in the hidden layer could be reduced from 7 neurons to 5 neurons while maintaining the same level of accuracy.

3.3. Temperature Estimation: Setup 2

The measurement data from Setup 2 aims to closely represent reality. For this purpose, EIS measurements were conducted at various temperatures and different SoC levels ranging from 10% to 90%. During the EIS measurements, the cells were charged or discharged with various currents with maximum C-rates of $\pm C/2$. Figure 13 displays the results of the temperature estimation. Again, impedance data for the entire frequency range between 10 kHz and 1 Hz and the SoC and DC current were provided to the ANN. The overall RMSE is below 0.9 K. The ANN utilized a hidden layer with 6 neurons.
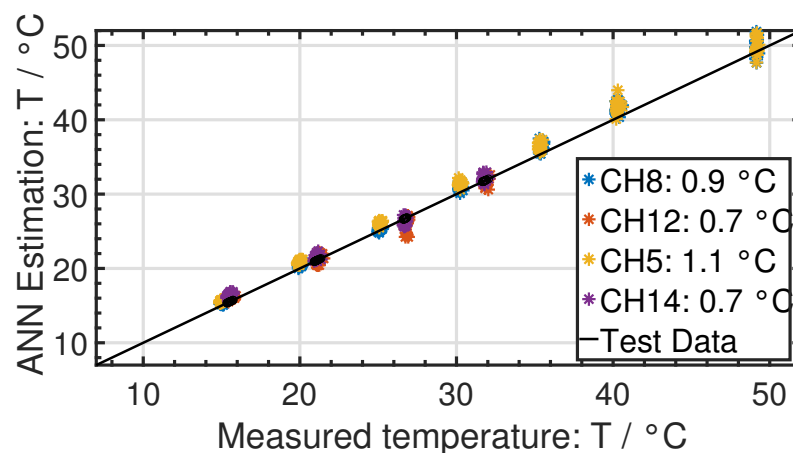
Figure 13. The plot displays the estimated temperature against the measured temperature, with a black line as a guide representing the target value. Various SoC and DC currents during the EIS measurements were investigated for data generation. The data from the entire frequency range were considered for the calculations. The overall RMSE for is less than 0.9 K. The legend indicates the RMSE for each individual cell.

Due to the significant increase in the measurement matrix resulting from the additional investigation of different SoC and DC currents at each temperature, the total number of examined temperatures had to be reduced. By conducting measurements at further temperatures, more data could be provided to the ANN, potentially improving its accuracy. Nevertheless, the results demonstrate that successful temperature determination in a multi-cell module under pseudo real conditions using impedance data processed with a simple ANN is achievable.

For this setup as well, the reduction of the frequency range was investigated. In this case, only impedance data for the frequencies between 800 Hz and 300 Hz was provided to the ANN. The results are presented in Figure 14.
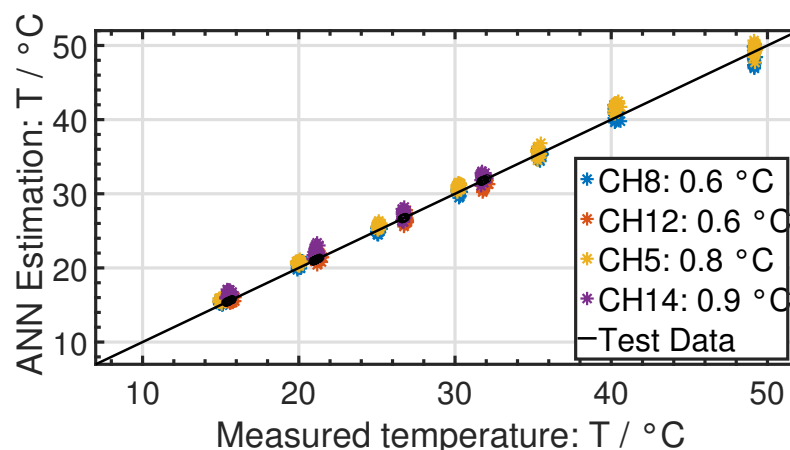
Figure 14. The plot displays the estimated temperature against the measured temperature, with a black line as a guide representing the target value. For the temperature calculation, only the data from the reduced frequency range of 800 Hz to 30 Hz were considered. The overall RMSE for is less than 0.8 K. The legend indicates the RMSE for each individual cell.

The overall RMSE is lower than 0.8 K. The accuracy of the estimation was even improved by reducing the impedance data. The number of neurons used in the ANN was reduced from 6 neurons to 5 neurons.

3.4. Further Discussion

For all the presented results, a Bayesian regularization-backpropagation ANN with one hidden layer is used. As input parameters, both the real and the imaginary part of the impedance and SoC and DC current are fed to the ANN. The training of the ANN can also be conducted without providing the SoC, but this leads to an increase in computational time during training while maintaining nearly the same accuracy. The influences of operating parameters (temperature, State of Charge, and DC current during EIS measurements) investigated in Section 3.1 reveal that the frequency range between 800 Hz and 30 Hz is particularly affected by temperature, while the State of Charge and DC current show almost no influence. Therefore, the number of used frequencies was reduced from 61 to 21, resulting in a reduction of the input parameters from 124 to 44 (21 real parts, 21 imaginary parts, SoC, and DC current). By reducing the number of frequencies, the measurement time is significantly decreased, resulting in a reduction of the required capacity for the EIS measurements. The applied AC current corresponds to a C-rate of C/20. With the reduced frequency range, it is possible to conduct the measurement in less than 0.5 s. If measurements are performed only every 10 s, the normalized continuous current required for the measurement methodology is reduced to a C-rate of C/400. It is evident that the presented method is only practical with cost-effective measurement technology. The potentiostat introduced in this study by Gamry is too expensive for real-world battery systems. Koseoglou et al. present an impedance measurement system in their study, where a sinusoidal alternating current is applied to a cell through discharge using a

MOSFET [36]. In a future study, this setup will be reconstructed and applied to a system of interconnected cells. The previously mentioned limitation of the required frequency range also represents a significant simplification for the hardware development of an impedance chip, as the demands on measurement accuracy increase with rising frequency. Furthermore, the reduction of input data significantly decreases the required computational power. A major advantage of the demonstrated temperature estimation using ANN is that the necessary computational power is very low once the ANN is trained. Indeed, this characteristic makes the approach even more attractive and practical for industrial applications. The ANN training process only takes a few minutes for each system. In further investigations, it will be determined whether the number of required frequencies can be further reduced. This could potentially lead to further reductions in measurement time and computational complexity.

As part of this study, an attempt was made to determine the SoC using the presented method. However, since the SoC, as demonstrated, has only a very limited influence on the impedance spectrum, convincing results could not be obtained in this regard.

The accuracy of the presented method for temperature estimation, with an average error of approximately 1 K and a maximum deviation between 2 K and 3 K, is comparable to the results found in the literature. Some literature reports even claim accuracy within 1 K, but these often pertain to static systems that are at equilibrium, with the entire cell having the same temperature. In contrast, in dynamic systems, it becomes a matter of definition to determine the temperature of the cell at any given moment, as different regions within the cell may have varying temperatures. In this study, the temperature was measured in the core of the cell, but the average temperature of the entire cell tends to be lower during dynamic operation.

For real-world applications, such as electric vehicles, an accuracy of 1 K or 2 K is perfectly adequate, as there is usually no practical distinction between a cell temperature of 50 °C or 52 °C. To make the methodology for temperature determination truly usable, other factors such as computational power become relevant. In an electric vehicle with hundreds to thousands of individual battery cells, it is crucial that determining the temperature of a single cell consumes minimal computational resources. This is where the presented methodology shines. Unlike most thermal models that require continuously sampling and processing time-series data, a single snapshot during an EIS measurement is sufficient. This significantly reduces data traffic. The use of a simple ANN with only one hidden layer has the advantage that it does not require solving partial differential equations or data fitting, thus keeping the computational demands very low. After the ANN is trained, its state estimation calculations are swiftly executed within milliseconds. Given its data-driven essence, we propose that this approach could be flexibly extended to other cell chemistries, provided a strong correlation between the EIS spectra and the target state can be established. The introduced ANN technique demonstrates noteworthy effectiveness, especially in elevated temperatures, where the influence of the DC current is lessened. This characteristic renders it exceptionally well-suited for real-world applications.

4. Conclusions

In this study, we introduced a sensorless approach for temperature prediction of lithium-ion cells using ANNs and electrochemical impedance spectroscopy as input data. The investigation was conducted on LG INR18650MH1 lithium-ion cylindrical cells, which were connected in a 3s2p configuration. Variations in the SoC and the application of superimposed DC current during EIS measurements were considered to simulate real-world scenarios. The overall RMSE for all temperature estimations was approximately 1 K, which underscores the appeal of the presented method for practical implementation. To further optimize the methodology, an analysis of the influence of temperature, SoC, and DC current on impedance at different frequencies was conducted. As a result of this analysis, the frequency range was reduced from the original 10 kHz to 1 Hz to a range of 800 Hz to 30 Hz. The number of frequencies for the impedance spectrum was reduced from 61 to 21, and the number of input neurons was reduced from 124 to 44.

The accuracy of temperature estimation was even improved to some extent by reducing the frequency range. At the same time, the time required for measurements and the computational efforts for the ANN were significantly reduced. The method presented here boasts several advantages when compared to other temperature estimation techniques. Firstly, this approach eliminates the need to fit a battery model to the data and avoids the necessity of solving differential equations. Additionally, the ANN solely relies on a single EIS spectrum to estimate cell temperature, obviating the handling of time series data. This predictive technique exhibits promise in accurately gauging internal cell temperature swiftly, demanding minimal measurement and computational resources.

Author Contributions: Conceptualization, M.S. and K.P.B.; methodology, M.S. and K.P.B.; investigation, M.S. and V.K.; writing—original draft preparation, M.S. and V.K.; writing—review and editing, K.P.B.; visualization, M.S.; supervision, K.P.B.; project administration, M.S.; funding acquisition, K.P.B. All authors have read and agreed to the published version of the manuscript.

References

1. Pevec, D.; Babic, J.; Podobnik, V. Electric vehicles: A data science perspective review. *Electronics* **2019**, *8*, 1190. [CrossRef]
2. Ma, S.; Jiang, M.; Tao, P.; Song, C.; Wu, J.; Wang, J.; Deng, T.; Shang, W. Temperature effect and thermal impact in lithium-ion batteries: A review. *Prog. Nat. Sci. Mater. Int.* **2018**, *28*, 653–666. [CrossRef]
3. Wang, Q.; Ping, P.; Zhao, X.; Chu, G.; Sun, J.; Chen, C. Thermal runaway caused fire and explosion of lithium ion battery. *J. Power Sources* **2012**, *208*, 210–224. [CrossRef]
4. Chen, M.; Dongxu, O.; Liu, J.; Wang, J. Investigation on thermal and fire propagation behaviors of multiple lithium-ion batteries within the package. *Appl. Therm. Eng.* **2019**, *157*, 113750. [CrossRef]
5. *GB 38031-2020*; National Standard of the People's Republic China (GB): Electric Vehicles Traction Battery Safety Requirements. Standardization Administration: Beijing, China, 2020; pp. 1–42.
6. Wang, Z.; Zhu, L.; Liu, J.; Wang, J.; Yan, W. Gas sensing technology for the detection and early warning of battery thermal runaway: A review. *Energy Fuels* **2022**, *36*, 6038–6057. [CrossRef]
7. Draft Global Technical Regulation on Electric Vehicle Safety. ECE/TRANS/WP.29/GRSP/2017/2. 2017. Available online: https://www.unece.org/fileadmin/DAM/trans/doc/2017/wp29grsp/GRSP-61-07.pdf (accessed on 17 August 2023).
8. Zheng, Y.; Che, Y.; Hu, X.; Sui, X.; Teodorescu, R. Sensorless Temperature Monitoring of Lithium-ion Batteries by Integrating Physics with Machine Learning. *IEEE Trans. Transp. Electrif.* **2023**. [CrossRef]
9. Wang, X.; Wei, X.; Chen, Q.; Zhu, J.; Dai, H. Lithium-ion battery temperature on-line estimation based on fast impedance calculation. *J. Energy Storage* **2019**, *26*, 100952. [CrossRef]
10. Mc Carthy, K.; Gullapalli, H.; Ryan, K.M.; Kennedy, T. Use of impedance spectroscopy for the estimation of Li-ion battery state of charge, state of health and internal temperature. *J. Electrochem. Soc.* **2021**, *168*, 080517. [CrossRef]
11. Li, D.; Wang, L.; Duan, C.; Li, Q.; Wang, K. Temperature prediction of lithium-ion batteries based on electrochemical impedance spectrum: A review. *Int. J. Energy Res.* **2022**, *46*, 10372–10388. [CrossRef]
12. Surya, S.; Marcis, V.; Williamson, S. Core temperature estimation for a lithium ion 18,650 cell. *Energies* **2020**, *14*, 87. [CrossRef]
13. Raijmakers, L.; Danilov, D.L.; Eichel, R.A.; Notten, P. A review on various temperature-indication methods for Li-ion batteries. *Appl. Energy* **2019**, *240*, 918–945. [CrossRef]
14. Richardson, R.R.; Ireland, P.T.; Howey, D.A. Battery internal temperature estimation by combined impedance and surface temperature measurement. *J. Power Sources* **2014**, *265*, 254–261. [CrossRef]
15. Li, Z.; Zhang, J.; Wu, B.; Huang, J.; Nie, Z.; Sun, Y.; An, F.; Wu, N. Examining temporal and spatial variations of internal temperature in large-format laminated battery with embedded thermocouples. *J. Power Sources* **2013**, *241*, 536–553. [CrossRef]
16. Richardson, R.R.; Howey, D.A. Sensorless Battery Internal Temperature Estimation using a Kalman Filter with Impedance Measurement. *IEEE Trans. Sustain. Energy* **2015**, *6*, 1190–1199. [CrossRef]
17. Liu, K.; Li, K.; Peng, Q.; Zhang, C. A brief review on key technologies in the battery management system of electric vehicles. *Front. Mech. Eng.* **2019**, *14*, 47–64. [CrossRef]

18. Lelie, M.; Braun, T.; Knips, M.; Nordmann, H.; Ringbeck, F.; Zappen, H.; Sauer, D. Battery Management System Hardware Concepts: An Overview. *Appl. Sci.* **2018**, *8*, 534. [CrossRef]

19. Liu, G.; Ouyang, M.; Lu, L.; Li, J.; Han, X. Analysis of the heat generation of lithium-ion battery during charging and discharging considering different influencing factors. *J. Therm. Anal. Calorim.* **2014**, *116*, 1001–1010. [CrossRef]

20. Xie, Y.; Li, W.; Hu, X.; Zou, C.; Feng, F.; Tang, X. Novel mesoscale electrothermal modeling for lithium-ion batteries. *IEEE Trans. Power Electron.* **2019**, *35*, 2595–2614. [CrossRef]

21. Pang, H.; Guo, L.; Wu, L.; Jin, J.; Zhang, F.; Liu, K. A novel extended Kalman filter-based battery internal and surface temperature estimation based on an improved electro-thermal model. *J. Energy Storage* **2021**, *41*, 102854. [CrossRef]

22. Srinivasan, R.; Carkhuff, B.G.; Butler, M.H.; Baisden, A.C. Instantaneous measurement of the internal temperature in lithium-ion rechargeable cells. *Electrochim. Acta* **2011**, *56*, 6198–6204. [CrossRef]

23. Schmidt, J.P.; Arnold, S.; Loges, A.; Werner, D.; Wetzel, T.; Ivers-Tiffée, E. Measurement of the internal cell temperature via impedance: Evaluation and application of a new method. *J. Power Sources* **2013**, *243*, 110–117. [CrossRef]

24. Wang, L.; Lu, D.; Song, M.; Zhao, X.; Li, G. Instantaneous estimation of internal temperature in lithium-ion battery by impedance measurement. *Int. J. Energy Res.* **2020**, *44*, 3082–3097. [CrossRef]

25. Beelen, H.; Mundaragi Shivakumar, K.; Raijmakers, L.; Donkers, M.; Bergveld, H.J. Towards impedance-based temperature estimation for Li-ion battery packs. *Int. J. Energy Res.* **2020**, *44*, 2889–2908. [CrossRef]

26. Beelen, H.; Raijmakers, L.; Donkers, M.; Notten, P.; Bergveld, H.J. A comparison and accuracy analysis of impedance-based temperature estimation methods for Li-ion batteries. *Appl. Energy* **2016**, *175*, 128–140. [CrossRef]

27. Feng, F.; Teng, S.; Liu, K.; Xie, J.; Xie, Y.; Liu, B.; Li, K. Co-estimation of lithium-ion battery state of charge and state of temperature based on a hybrid electrochemical-thermal-neural-network model. *J. Power Sources* **2020**, *455*, 227935. [CrossRef]

28. Hasan, M.M.; Ali Pourmousavi, S.; Jahanbani Ardakani, A.; Saha, T.K. A data-driven approach to estimate battery cell temperature using a nonlinear autoregressive exogenous neural network model. *J. Energy Storage* **2020**, *32*, 101879. [CrossRef]

29. Eddahech, A.; Briat, O.; Bertrand, N.; Delétage, J.Y.; Vinassa, J.M. Behavior and state-of-health monitoring of Li-ion batteries using impedance spectroscopy and recurrent neural networks. *Int. J. Electr. Power Energy Syst.* **2012**, *42*, 487–494. [CrossRef]

30. Yang, D.; Wang, Y.; Pan, R.; Chen, R.; Chen, Z. A Neural Network Based State-of-Health Estimation of Lithium-ion Battery in Electric Vehicles. *Energy Procedia* **2017**, *105*, 2059–2064. [CrossRef]

31. You, G.W.; Park, S.; Oh, D. Diagnosis of Electric Vehicle Batteries Using Recurrent Neural Networks. *IEEE Trans. Ind. Electron.* **2017**, *64*, 4885–4893. [CrossRef]

32. Tong, S.; Lacap, J.H.; Park, J.W. Battery state of charge estimation using a load-classifying neural network. *J. Energy Storage* **2016**, *7*, 236–243. [CrossRef]

33. Messing, M.; Shoa, T.; Ahmed, R.; Habibi, S. Battery SoC Estimation from EIS using Neural Nets. In Proceedings of the 2020 IEEE Transportation Electrification Conference & Expo (ITEC), Chicago, IL, USA, 23–26 June 2020; pp. 588–593. [CrossRef]

34. Ströbel, M.; Pross-Brakhage, J.; Kopp, M.; Birke, K.P. Impedance based temperature estimation of lithium ion cells using artificial neural networks. *Batteries* **2021**, *7*, 85. [CrossRef]

35. Kopp, M.; Ströbel, M.; Fill, A.; Pross-Brakhage, J.; Birke, K.P. Artificial feature extraction for estimating state-of-temperature in lithium-ion-cells using various long short-term memory architectures. *Batteries* **2022**, *8*, 36. [CrossRef]

36. Koseoglou, M.; Tsioumas, E.; Papagiannis, D.; Jabbour, N.; Mademlis, C. A novel on-board electrochemical impedance spectroscopy system for real-time battery impedance estimation. *IEEE Trans. Power Electron.* **2021**, *36*, 10776–10787. [CrossRef]